

Thermal and Structural Properties of Ethylammonium Chloride and Its Mixture with Water

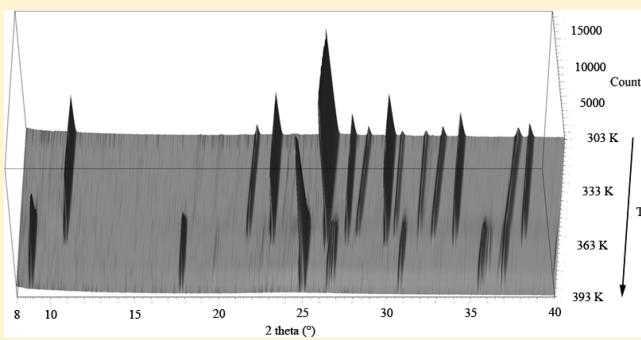
Valentina Migliorati,[†] Paolo Ballirano,^{*,‡} Lorenzo Gontrani,[†] Alessandro Triolo,[§] and Ruggero Caminiti[†]

[†]Dipartimento di Chimica, and [‡]Dipartimento di Scienze della Terra, Sapienza Università di Roma, Piazzale Aldo Moro 5, I-00185 Roma, Italy

[§]Consiglio Nazionale delle Ricerche, Istituto di Struttura della Materia, Area di Tor Vergata, Via del Fosso del Cavaliere 100, I-00133 Roma, Italy

 Supporting Information

ABSTRACT: The temperature dependence of ethylammonium chloride structure has been investigated by *in situ* laboratory parallel-beam X-ray powder diffraction. A polymorphic transition from a monoclinic LT phase to a tetragonal HT phase has been observed at 358 K. Such transformation has a reconstructive character. The thermal expansion of both polymorphs is small and anisotropic as a consequence of their organization through an anisotropic interaction network. The high temperature (HT) phase (possible space group $P4/n$ or $P4/nmm$, $a = 5.05 \text{ \AA}$, $c = 9.99 \text{ \AA}$) has an excess volume of $\sim 11\%$ as compared with the low temperature (LT) one. The HT polymorph's structure has been solved by direct methods using powder diffraction data. In the absence of clear indications, it has been refined in $P4/nmm$. The structural properties of an ethylammonium chloride/water mixture at ambient conditions were also studied by using an integrated approach, which combines X-ray diffraction measurements and molecular dynamics simulations carried out with both the SPC/E and TIPSP water models. By refining a single interaction potential, very good agreement between the theoretical and experimental diffraction patterns was obtained, especially in the case of the TIPSP simulation. A complex structural behavior in which cations and anions do not possess a completely closed hydration shell of their own has been highlighted. Conversely, “solvent-shared ion pairs” are formed, in which one or more water molecules act as a bridge between the chloride and ethylammonium ions. Moreover, a strong water–water correlation is found, indicating that the water molecules in the mixture tend to aggregate and form water clusters.



INTRODUCTION

Ionic liquids (ILs) are attracting increasing attention because of their importance as potential nonvolatile solvents in green chemistry and liquid electrolytes.^{1,2} Moreover, they are candidates as materials used for thermal energy storage. Therefore, studies on the thermal stability of such materials are rapidly increasing because of the wide range of applications of these materials. In the framework of a broader investigation on the thermal stability of $C_nH_{2n+1}NH_3Cl$ ($n = 1, 2, 3$, etc.) ILs, ethylammonium chloride (EAC, $C_2H_5NH_3Cl$) has especially attracted our attention. Strictly speaking, EAC should not be considered as an IL, if we adopt the IL definition that restricts this term to salts whose melting point is below 373 K (EAC melts at about 383 K). However, it does come under the broader definition since it is a “low melting” salt. Its melting point is by far closer to 373 K than to the melting temperatures of other molten salts that are usually very high (above 473 K).

Despite the reported difficulty in growing single crystals of adequate quality^{3,4} EAC structure has been recently determined⁵ and proved to be isostructural with that of other ethylammonium

halides,⁶ monoclinic system s.g. $P2_1/m$. Two different modifications have been reported for both $C_2H_5NH_3Br$, and $C_2H_5NH_3I$ above room temperature (RT), whereas no phase transitions were detected for EAC up to the melting point at 369 K.^{6–8} Subsequently, a more recent work,⁴ from temperature-dependent Raman spectroscopy data, reported the occurrence of a phase transition at 345 K signaled by many spectral anomalies. The author concluded indicating the presence of an order–disorder transition. Moreover, the possible occurrence of a high-temperature cubic-prototype phase, similar to that found in alkali thiocyanides,⁹ was proposed. However, the lack of crystallographic information prevented the author from providing a more detailed description of the phase transition.

A recent report¹⁰ focused on both phase diagram and dynamics in ethylammonium halides (Cl, Br, and I). The study, which was based on both DSC and NMR experiments, highlights

Received: January 31, 2011

Revised: March 21, 2011

Published: April 12, 2011

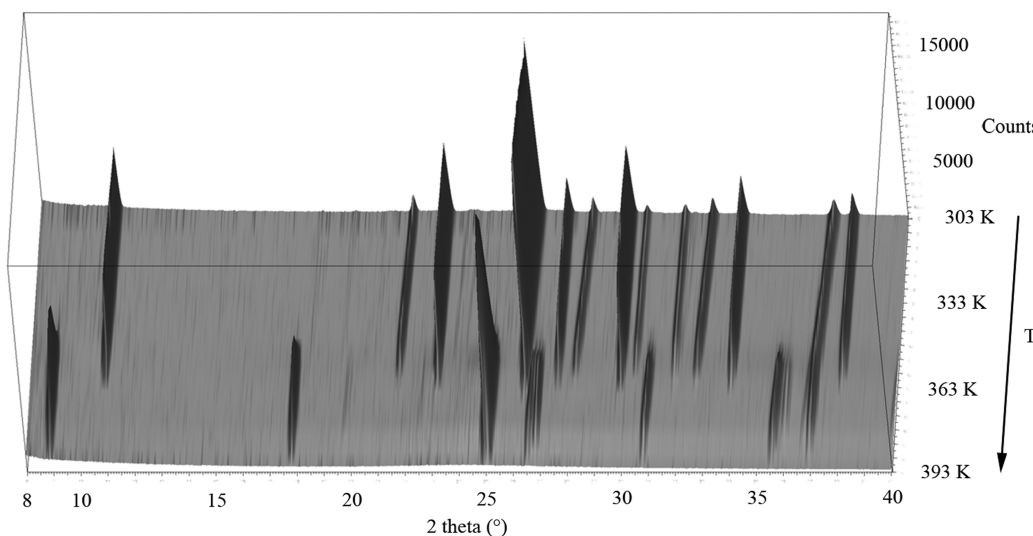


Figure 1. Magnified view (8 – $40^\circ 2\theta$) of the full data set of the heating cycle of the title compound.

several important issues: (a) The chloride and bromide salts are characterized by the same phase transitions; the RT-stable phase (hereinafter referred to as the β -phase) shows a transition toward a new crystalline phase (hereinafter indicated as the α -phase). At higher temperature, the α -phase melts into an isotropic phase. For the case of the chloride, the $\beta \rightarrow \alpha$ transition occurs at 357.4 K, whereas the $\alpha \rightarrow$ isotropic transition occurs at 383.4 K. (b) Below RT, only methyl and ammonium group reorientational motions take place. Above the $\beta \rightarrow \alpha$ transition temperature, the whole molecule rotates about an n -fold axis ($n > 2$). In the case of chloride, a rotation axis in the plane perpendicular to the bisector of the H—C—H bond angle of the methylene unit (model 2) provided the best fit of NMR data. In contrast, model 1, consisting of a rotation about an axis lying in the molecular mirror plane, provided the best fit for both bromide and iodide salts, despite the supposed isostructural among the three ethylammonium halides. (c) The activation energies for the ammonium reorientation reflect decreasing hydrogen bond strength (Cl > Br > I).

In addition to the crystal polymorphism of ILs, another aspect of great interest is their behavior in mixtures with other solvents, such as water. The significance of the interaction between ILs and water has been well-recognized for many reasons. For example, most ILs are hygroscopic and absorb water vapor from the atmosphere. The presence of water can dramatically affect the physical properties of ILs, such as their polarity, viscosity, and conductivity, even at low concentrations.¹¹ The water content of mixtures can also affect the rates and selectivity of reactions carried out in ILs.¹² Moreover, one of the most promising applications of ILs is as green solvents and, in this respect, the solubility of these systems in water can be an important factor. Indeed, one potential problem of using ILs as solvents is the possible pathway into the environment through wastewater.¹³ Therefore, it is fundamental to gain a molecular level understanding of ILs/water mixtures. A considerable number of experimental and theoretical studies have recently been published on the interaction between imidazolium based ILs and water.^{14–19}

In ILs consisting of anions with a strong ability to form hydrogen bonds, such as $[\text{NO}_3]^-$ and $[\text{CF}_3\text{CO}_2]^-$, water

molecules were found to be mainly hydrogen-bonded to the anion,¹⁴ but some author has also inferred a weak C—H \cdots O interaction of water with the most “acidic” ring proton of imidazolium-based ILs.^{15,16} Complex behavior has been reported in some cases. For example, in a study of 1-butyl-3-methylimidazolium tetrafluoroborate/water mixtures, Schröder et al. found that the effect of water on the ionic liquid structure is not an “interstitial effect” that weakens the cation—anion network, but rather, the impact of water shows up in a blurring of the anion–cation orientational structure with increasing water content.¹⁷

Hanke and Lynden-Bell instead studied mixtures with water of 1,3-dimethylimidazolium chloride and of 1,3-dimethylimidazolium hexafluorophosphate, and they found the formation of networks of water molecules as well as isolated clusters at high water concentrations.¹⁸ Despite this extensive research activity, to date, a detailed molecular level understanding of the interactions between water and ILs is still lacking. This is due to the fact that study of the structural and dynamic properties of disordered systems, such as ILs/water mixtures, is a complex task, and it is very difficult to obtain accurate information, especially when using a single method of investigation. The combination of experimental and theoretical techniques is thus essential to obtain reliable results on these systems, and among other approaches, the combined use of simulation methods and X-ray diffraction techniques has been shown to be particularly well-suited to provide a reliable description of liquid samples.²⁰

The present contribution has two main objectives. First, it is aimed at providing the crystallographic data required for a complete understanding of the structural modifications occurring during heating of EAC from RT to the melting point. After several unsuccessful attempts to grow single crystals of dimension and quality adequate for conventional crystallographic analysis we decided to carry out an *in situ* laboratory parallel-beam X-ray powder diffraction investigation to achieve this task. The second aim of this work is the study of the structural properties of an EAC/water mixture, by combining fully atomistic molecular dynamics (MD) simulations and high-energy X-ray diffraction experiments. To the best of our knowledge, no investigation has been carried out until now on mixtures of water and ethylammonium halides.

METHODS

X-ray Powder Diffraction Measurements. Powder of the title compound was loaded and packed in a 0.7-mm-diameter borosilicate glass capillary that was subsequently sealed. The sample, Fluka 02960 p.a., was used without any further purification. The capillary was glued to a 1.2-mm-diameter Al_2O_3 tube by means of a high-purity alumina ceramic (Resbond 989). The capillary/tube assembly was subsequently aligned onto a standard goniometer head, and diffraction data were collected on a parallel-beam Bruker AXS D8 Advance, operating in transmission in $\theta-\theta$ geometry. The instrument is fitted with a PSD Väntec-1 detector set to a 6° 2θ aperture and with a prototype of capillary heating chamber.^{21–25} Data were measured in the 8 – 90° 2θ angular range, step size 0.0219° 2θ , and 5 s counting time, using $\text{Cu K}\alpha$ radiation. Isothermal measurements were carried out in the 303 – 393 K thermal range with temperature steps of 5 K. A magnified view of the complete data set, consisting of 19 diffraction patterns, is shown in Figure 1.

A phase transition (corresponding to the $\beta \rightarrow \alpha$ transition proposed by Radcliffe¹⁰) was observed at 358 K, whereas the melting process started at 383 K and was detected from an abrupt increase of the background counterbalanced by a strong general intensity reduction of the Bragg reflections. Such process reached completion at 388 K.

Data were evaluated with the GSAS suite of programs²⁶ coupled with the EXPGUI graphical user interface.²⁷ Starting structural data, including hydrogen atoms' positions, were taken from ref 5. A structure refined at a given temperature was used as input for the subsequent temperature. Peak shapes were modeled by a pseudo-Voigt function modified to incorporate asymmetry.^{28,29} The peak cutoff was set to 0.1% of the peak maximum, and the background was fit with a 30-term Chebyshev polynomial of the first kind. Such a large number of parameters were required to properly model the contribution of the capillary. A total of 25 restraints on intramolecular bond distances and angles involving hydrogen atoms (expressed as pseudobonds) were imposed to obtain a better estimate of their position.³⁰ Moreover, N–C and C–C distances were restrained in the $1.49(1)$ and $1.52(1)$ Å ranges. Statistical associated weight was set to 10. Restraints contribution to χ^2 never exceeded 0.4%, indicating a proper weighting scheme. Isotropic displacement parameters were refined, constraining those of the atoms of N and C atoms of the cation to be equal (U_{iso} hydrogen = $1.5 \times U_{\text{iso}}$ non-hydrogen). Such simplification was adopted to reduce the number of refined parameters. An absorption measurement has been carried out collecting the transmitted beam through the sample $I_t(E)$ and the incident primary beam, $I_0(E)$, both in direct transmission. The derived μ_{eff} was found to be very small, and for this reason, no absorption correction was applied during the refinement.

An evaluation of texture was carried out by means of a generalized spherical-harmonic description³¹ up to the spherical harmonic order of four, including eight refinable l, m, n terms (2, 0, $\bar{2}$; 2, 0, 0; 2, 0, 2; 4, 0, $\bar{4}$; 4, 0, $\bar{2}$; 4, 0, 0; 4, 0, 2; 4, 0, 4). As expected for a capillary mount, an almost complete absence of preferred orientation was observed as a result of calculated texture indices J , close to 1 (range 1.0175–1.0262). During the final refinement cycles, the coefficients of the various l, m, n terms were kept fixed to the corresponding mean values, as calculated from the 19 diffraction patterns (corresponding to an average $J = 1.0209$).

Table 1. Miscellaneous Data of the Various Rietveld Refinements^a

Rp (%)	4.43–4.63
Rwp (%)	5.78–6.08
$R_{\text{F}2}$ (%)	6.15–7.07
χ^2	1.87–2.05
refined parameters	63 (30 background)
restraints	27
contribution of restraints to χ^2 (%)	0.16–0.34
J	1.021 (averaged)

^a Statistics indicators as defined by ref 32.

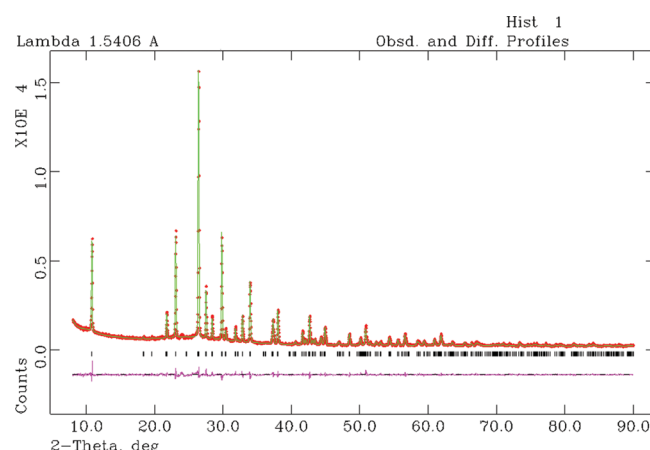


Figure 2. Fitted X-ray powder diffraction pattern obtained at 303 K.

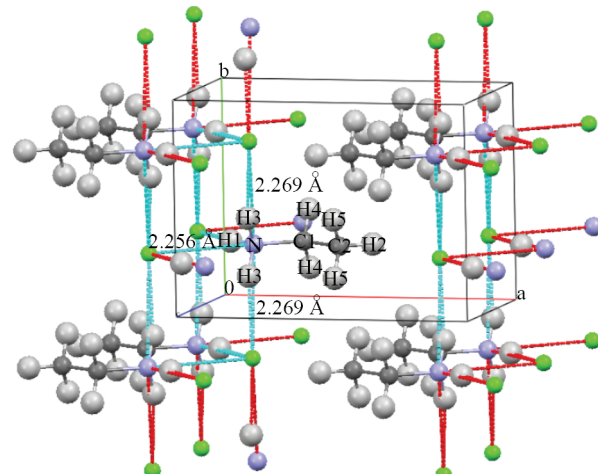


Figure 3. The packing of the LT polymorph of $\text{C}_2\text{H}_5\text{NH}_3\text{Cl}$ (Mercury 2.3).⁵³

Miscellaneous data of the various refinements are reported in Table 1. An example of the Rietveld plots obtained for the diffraction pattern collected at 303 K is reported in Figure 2. CIF files are available as Supporting Information.

For the HT polymorph, 11 peaks were located by a profile-fitting technique using the Topas 4.2 software.³³ Autoindexing was performed using TREOR90.³⁴ A solution was obtained in the tetragonal system for the following cell parameters: $a = 5.033(1)$ Å,

$c = 9.979(3)$ Å, and volume $272.78(1)$ Å³ and the following figures-of-merit: $M_{11} = 75$ and $F_{11} = 60(0.0123, 15)$.^{35,36} The reported volume is consistent with $Z = 2$. A LeBail fitting carried out with Topas 4.2 pointed out to the reflection condition $0k0$ for $k = 2n$ and $hk0$ for $h + k = 2n$, consistent with the extinction symbol $Pn\bar{a}$. Therefore, candidate space groups were $P4/n$, or $P4/nmm$.

X-ray Scattering Measurements. The ionic liquid EAC was dried in vacuum for about 48 h. The EAC/water mixture was then prepared by adding a weighted amount of freshly distilled water to a weighted amount of solid EAC in a round-bottomed flask, thus obtaining an EAC/water molar ratio of 1:7.51. The choice of this molar ratio is motivated by the fact that we intend to study the structural properties of the mixture for an intermediate concentration of water, at which the water molecules are neither in deficiency nor in great excess as compared with the number of ion pairs. Since the hydration number of Cl⁻ in aqueous solution is 6 (vide infra), 7.51 water molecules are supposed to be enough to saturate the anion coordination sphere. The density of the mixture was 1.03 g/cm³. The sample was rapidly transferred into a cell sealed with Mylar windows. Sample and windows thicknesses were 3 mm and 6 μm, respectively. The large angle X-ray scattering experiments were conducted using the noncommercial energy-scanning diffractometer built in the Department of Chemistry, Rome University "La Sapienza" (Italian Patent no. 01126484; June 23, 1993; R. Caminiti et al.^{37,38}). White Bremsstrahlung radiation emitted by a tungsten tube operating at 50 kV and 40 mA was used. Scattered intensities for the sample and the empty cell were measured at eight different angles (24.0, 15.5, 8.0, 3.0, 2.0, 1.5, 1.0, and 0.5°). This choice allows covering a wide range of the momentum transfer, Q ; namely, between 0.12 and 19.56 Å⁻¹.

The expression for Q is

$$Q = \frac{4\pi \sin \theta}{\lambda} = 1.014E \sin \theta$$

where 2θ is the scattering angle, and E is expressed in keV, and Q in Å⁻¹. The primary beam intensity $I_0(E)$ was experimentally measured by reducing the tube current to 10 mA without the sample. Transmission of the sample was measured under the same conditions. Both quantities are needed to carry out the necessary absorption corrections to experimental data. The ultrathin Mylar cell windows' contribution to the diffraction intensity is less than 1/10 000 of the total. The diffracted intensities recorded at the various angles were normalized to a stoichiometric unit of volume and merged to yield the total static structure factor $I(Q)$, which is given by

$$I(Q) = I_{eu}(Q) - \sum_{i=1}^N x_i f_i^2$$

where $I_{eu}(Q)$ is the observed diffracted intensity in electron units, and x_i and f_i are the numerical concentrations of the atoms and their scattering factors. This function was multiplied by Q and by a Q -dependent sharpening factor, $M(Q)$,

$$M(Q) = \frac{f_N^2(0)}{f_N^2(Q)} e^{-0.01Q^2}$$

having chosen nitrogen as the sharpening atom. This procedure enhances the resolution of the curve at high Q values and decreases the truncation error in the calculation of the Fourier

transform from reciprocal (Q) to direct space (r). The structure function $I(Q)$ has been Fourier-transformed into a radial distribution function ($D(r)$), according to the relation

$$D(r) = 4\pi r^2 \rho_0 + \frac{2r}{\pi} \int_0^{Q_{max}} Q I(Q) M(Q) \sin(rQ) dQ$$

where ρ_0 is the system density and Q_{max} is the highest measured Q value (19.56 Å⁻¹).

If the uniform distribution component is dropped, which corresponds to the term $4\pi r^2 \rho_0$, we obtain the differential correlation function, $\text{Diff}(r)$, which contains only the structural contribution to the distribution function. For a detailed discussion of the experimental data treatment, see refs 39–41.

Molecular Dynamics simulation Details. The MD simulations of the EAC/water mixture were carried out using the DL_POLY package.⁴² The system was composed of 343 ion pairs and 2576 water molecules (the same molar ratio 1:7.51 used in the experiments) and was placed in a cubic box of 49.3 Å edge, with periodic boundary conditions. The partial charges of the EA cation were calculated with Gaussian 03⁴³ using the CHPGP procedure⁴⁴ at the MP2/cc-pVTZ (-f)//HF/6-31G(d) level. All of the other force field parameters for EAC were taken from the Lopes and Padua force field.^{45,46} For water, two of the most widespread water models were employed; namely, the SPC/E⁴⁷ and TIPSP.⁴⁸ The fundamental difference between these models is that although SPC/E is a three-site model with the negative charge on the oxygen atom, TIPSP is a five-site model in which the oxygen is neutral and the negative charge is placed on two massless dummy atoms located orthogonal to the water plane.

In the first step of our analysis, two MD simulations were carried out using the SPC/E and TIPSP water models in which the Lennard-Jones parameters for all of the unlike atoms were obtained from the Lorentz–Berthelot combining rules. In a second step, one Lennard-Jones parameter for the Cl–water interaction has been optimized to improve the description of the experimental data. The initial configurations were constructed by positioning the ions and the water molecules on selected lattice positions within a very large cubic simulation box. Extensive equilibration runs have been performed, comprising 10 000 steps of initial energy minimization, a short NPT run at 500 K and 10 atm aimed at randomizing the system, followed by another NPT run at 300 K and very high pressure (100 atm) to compress the box volume until the experimental density was reached (1.03 g/cm³). Then the systems were equilibrated under constant NVT conditions ($T = 300$ K and $P = 1$ atm) for about 0.5 ns. The production runs were carried out in the NVT ensemble for 2 ns, with a time step of 1 fs and saving a configuration every 100 timesteps. The temperature was kept constant at 300 K using the Nosé–Hoover thermostat^{49,50} with a relaxation constant of 0.5 ps. A cutoff of 8 Å was used to deal with nonbonded interactions, with the Ewald summation method to treat long-range electrostatic effects. All the bonds involving hydrogen atoms were constrained using the SHAKE algorithm.

The theoretical structure factors $I(Q)$ have been calculated from the MD simulations by using the following equation:⁵¹

$$I(Q) = \sum_{i=1}^N \sum_{j=1}^N x_i x_j f_i f_j H_{ij}(Q)$$

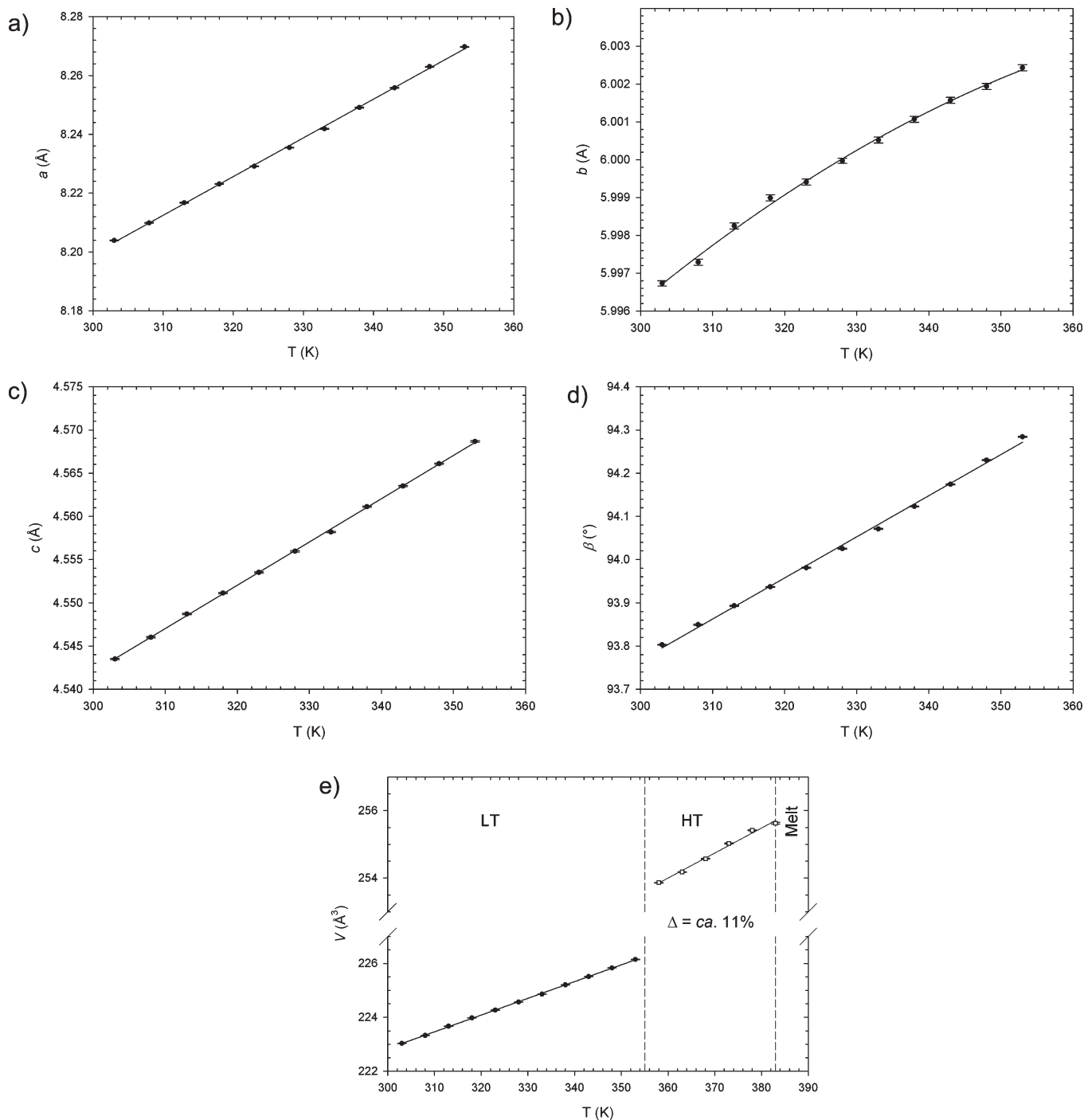


Figure 4. Evolution of cell parameters and volume with temperature: (a) a cell parameter, (b) b cell parameter, (c) c cell parameter, (d) β angle, and (e) volume.

where H_{ij} are the partial structure factors, defined in terms of the radial distribution functions by the Fourier integral:

$$H_{ij}(Q) = 4\pi\rho_0 \int_0^{r_{\max}} r^2 (g_{ij}(r) - 1) \frac{\sin(Qr)}{Qr} dr$$

where ρ_0 is the bulk number density of the system and r_{\max} is half the box edge.

The partial structure factors have been computed using the standard GROMACS tool `g_rdf`⁵² and the theoretical structure factors have been calculated with an in-house written code. The

theoretical $I(Q)$ was then multiplied by Q and by the same sharpening factor used for the experimental data to obtain a theoretical $QI(Q)M(Q)$ function that can be directly compared with the experimental data. The theoretical $\text{Diff}(r)$ functions were also calculated as described before.

RESULTS AND DISCUSSION

Crystal Polymorphism of EAC. As expected, the refinement at 303 K resulted in a structure extremely similar to that reported by reference data⁵ at room temperature (Figure 3).

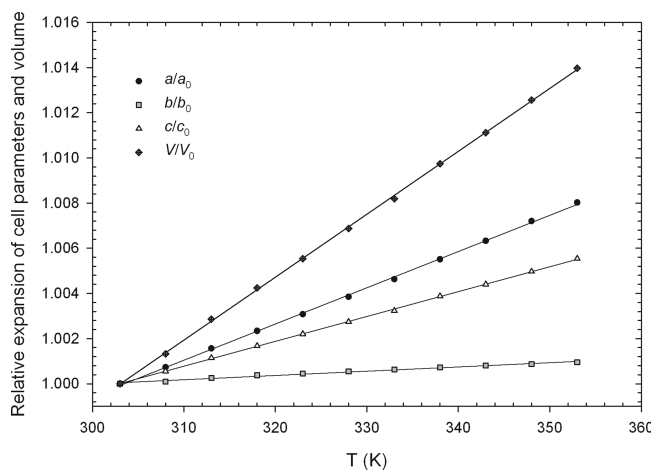


Figure 5. Relative expansion of cell parameters and volume with temperature.

The structure can be described in terms of double sheets running parallel to (100). Sheets are built up by linking anions and cations via N–H \cdots Cl interactions. Two interactions, involving N–H3 \cdots Cl, are predominantly aligned along b , whereas N–H1 \cdots Cl has a significant component parallel to c . The three distances are within the 2.25–2.27 Å range (N \cdots Cl \sim 3.2 Å) and are shorter than the corresponding 2.4 Å reported for C₂H₅NH₃Br.⁶ Similarly, the N–H1–Cl and N–H3–Cl angles are of \sim 164° and 157°, to be compared to 169° and 160° for C₂H₅NH₃Br. A fourth N \cdots Cl interaction at 3.25 Å occurs. It forms an angle of \sim 80° with the plane where the three N–H \cdots Cl bridges lie and shows all the features of an ionic interaction. Therefore, there is a lack of significant interaction along the a axis, a part of weak van der Waals forces. Evolution of cell parameters and volume with temperature are reported in Figure 4, and the corresponding relative expansion, in Figure 5.

According to the present results, thermal expansion is significantly anisotropic, albeit extremely limited, following the $\alpha_a > \alpha_c \gg \alpha_b$ trend. The β angle increases, as well. Within the investigated thermal range, the largest thermal expansion, shown by the a cell parameter, is of 0.8% only. The dependence of the unit cell parameters and volume from temperature have been empirically fitted with a second-order polynomial of type $p = a_0 + a_1 T + a_2 T^2$ where a_0 is the value of the corresponding parameter at 0 K, a_1 is the first-order coefficient of expansion, a_2 is the second-order coefficient, and T is the temperature in K.⁵⁴ However, only the b axis dependence departs significantly from linearity. Results from data-fitting are reported in Table 2.

A careful scrutiny of the structural modifications induced by heating reveals that the double sheet behaves as a substantially rigid unit. No variation on intramolecular bond distances as well as very marginal differences in the N–H3 \cdots Cl and N–H1 \cdots Cl contacts were detected. However, on the basis of the very limited thermal expansion, a maximum elongation of a few hundredths of Ångstroms is expected, a value that is not far away from the 3 times standard deviation significance level of the determined bond distances. Moreover, a very limited decrease of the N–H1–Cl angle from \sim 164 to \sim 162° has been observed, whereas N–H3–Cl is virtually unchanged. Therefore, it is reasonable to hypothesize that it is the weakening of the van der Waals interactions, prevalently acting along a , that provokes such anisotropy in the thermal expansion of EAC.

As expected, a fairly regular increase in the displacement parameters of both anion and cation atoms is observed throughout the investigated thermal range (Figure 6). Minor scattering is possibly due to correlation between the two parameters, as can be deduced from a scrutiny of the plot that shows an antiphase behavior of deviations from linearity at the same temperature (i.e., negative deviations from linearity of cation atoms, U_{iso} , are counterbalanced by a positive one of the anion, U_{iso}).

At the transition temperature, the cell volume undergoes a relevant expansion of \sim 11%. Such behavior is not unusual; it has been reported, for example, for ND₄NO₃.⁵⁵ This is clearly due to a less efficient packing of the HT polymorph. Such discontinuity is not consistent with an order–disorder transition, as hypothesized in reference data.⁴ Integrated intensities were extracted by the EXPO software⁵⁶ and subsequently used for ab initio direct methods structure solution using the SIR97 software.⁵⁷ Trials were performed in both possible space groups, P4/n and P4/nmm. However, the best final E maps for each space groups provided similar R values. The location of Cl, N, and C2 was consistently found at the same site (0, 1/2, $\pm z$), whereas the remaining carbon atom C1 was found to be rotationally disordered around the N–C2 vector. Considerations about sites multiplicity and geometry of NH₃ seem to point to P4/n as the correct space group. However, no hydrogen atoms were included in the refinement because of the expected extended disorder. Therefore, because of the absence of clear indications, refinements of the structure were carried out in the centrosymmetric P4/nmm space group (origin choice 2).

The derived fractional coordinates from direct methods were used as starting values for the refinement of the structure with the GSAS suite of program. The 22–23.5° 2θ angular range, where no reflections of the HT polymorph occur, was omitted because of the presence of the weak Cu K β component of the strong 110 reflection. This was due to a slight misalignment of the Göbel mirror that provides the parallel beam. Bond distances were restrained, similarly to the LT polymorph, imposing N–Cl = 1.47(1) Å, C1–C2 = 1.54(1) Å, and N–C2 2.46(2) Å and a statistical associated weight of 10. A very good fit ($R_{\text{F}2} = 0.108$) was therefore obtained (Figure 7), despite the lack of the hydrogen atoms, by locating the C2 atom at x, x, z with 25% occupancy.

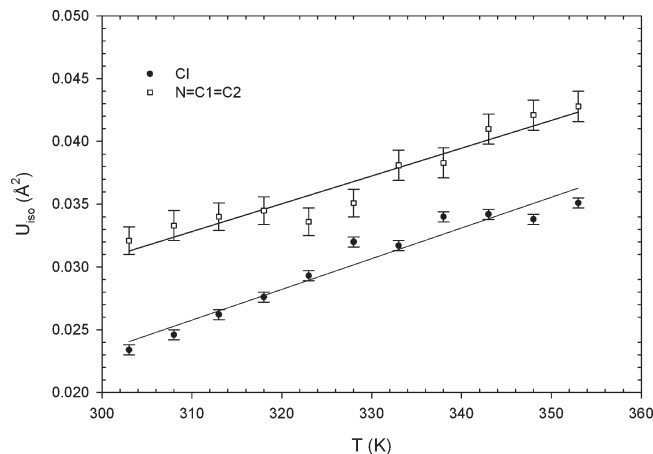
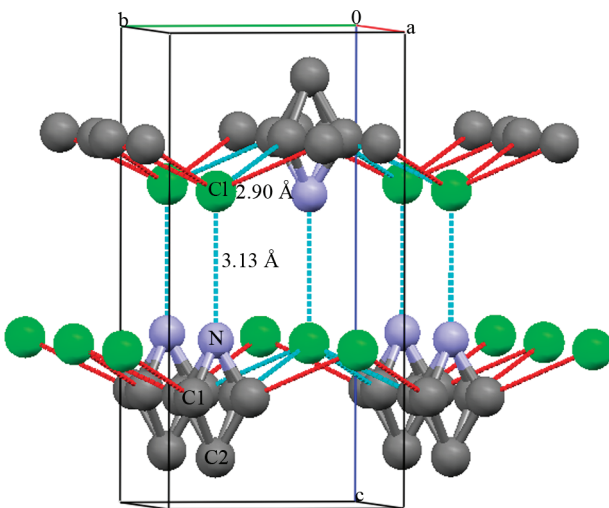
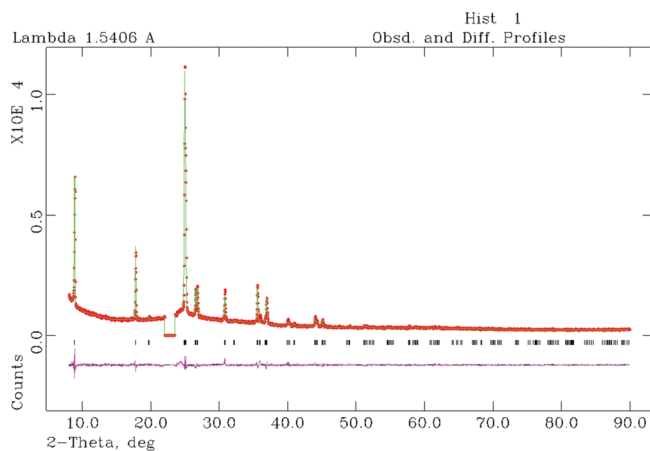
The relevant feature of the packing is an N \cdots Cl contact, aligned along the c axis, at 3.13 Å, a distance that is comparable with those observed in the LT polymorph. Moreover, four possible C1–Cl contacts at 2.90 Å as a result of the 4-fold symmetry are observed (Figure 8). However, because of the proposed disorder pattern (only one of the four C1 atom is present), zero, one, or two of them can statistically occur for each chlorine atom.

Those general features seem to be, at least partly, consistent with the anomalous behavior of the dependence of the cell parameters from temperature. In fact, the present data show a fairly linear increase in the cell volume for the HT polymorph (Figure 4e). However, the volume expansion is the result of an increase in the a and a reduction of the c parameters (Figure 9). It is worth noting that the N \cdots Cl interaction is aligned along the latter axis.

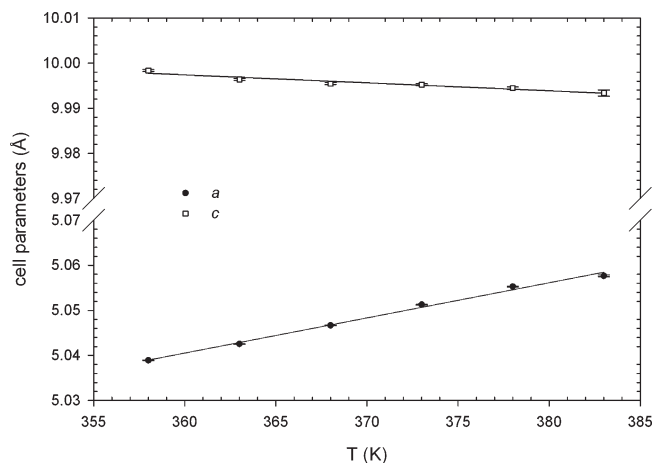
Structural Properties of the EAC/Water Mixture. The structural properties of the EAC/water mixture have been investigated by combining MD simulations and X-ray diffraction experiments. As previously mentioned, in the first step of our analysis, we have carried out two MD simulations of the EAC/water system, with the SPC/E and TIP5P water models, by using

Table 2. Results from Data-Fitting Procedure Using the Polynomial $p = a_0 + a_1T + a_2T^2$

	a (\AA)	b (\AA)	c (\AA)	β (deg)	volume (\AA^3)
R^2	0.9994	0.9978	0.9997	0.9979	0.9998
a_0	7.805(3)	5.88(1)	4.3920(9)	90.91(5)	204.2(1)
a_1	$1.32(1) \times 10^{-3}$	$6.2(9) \times 10^{-4}$	$5.00(3) \times 10^{-4}$	$9.5(1) \times 10^{-3}$	$6.21(3) \times 10^{-2}$
a_2		$-8(1) \times 10^{-7}$			

**Figure 6.** Evolution with temperature of isotropic displacement parameters U_{iso} for the non-hydrogen atoms of the cation and the chlorine ion.**Figure 8.** Molecular packing of the HT polymorph (Mercury 2.3).⁵³**Figure 7.** Fitted X-ray powder diffraction pattern obtained at 373 K.

the force field parameters reported in the literature (see the Methods section). The comparisons between the experimental structure factor $I(Q)$ and the theoretical ones calculated from the two MD simulations are shown in Figure 10a and b. The experimental $I(Q)$ is characterized by a principal double peak, whose peak positions are found at 1.95 and 2.72\AA^{-1} , followed by two less intense peaks centered at 4.60 and 6.52\AA^{-1} , and some less-well-defined oscillations beyond. As far as the SPC/E water model is concerned, the agreement between the theoretical and experimental $I(Q)$ s is not good, especially in the range between 4 and 12\AA^{-1} , where the theoretical peaks are shifted toward larger Q values and have a higher intensity as compared with the experimental ones. Even if a better agreement between theory

**Figure 9.** Evolution of cell parameters with temperature of the HT polymorph.

and experiment is found with the TIPSP water model, also in this case, the experimental pattern of peak positions and intensities is not correctly reproduced.

To clarify the origin of these discrepancies, it is extremely useful to compare the theoretical and experimental $\text{Diff}(r)$ functions in distance space (Figure 10c and d). Beyond the distance range between 0.0 and about 2.3\AA , where the $\text{Diff}(r)$ is due to intramolecular interactions and is correctly reproduced by our simulations, noticeable differences can be observed in all the distance range for both water models. In the experimental $\text{Diff}(r)$ function, three main peaks are found, centered at 3.15 , 4.80 , and 7.22\AA . The second and third peaks originate from medium-range

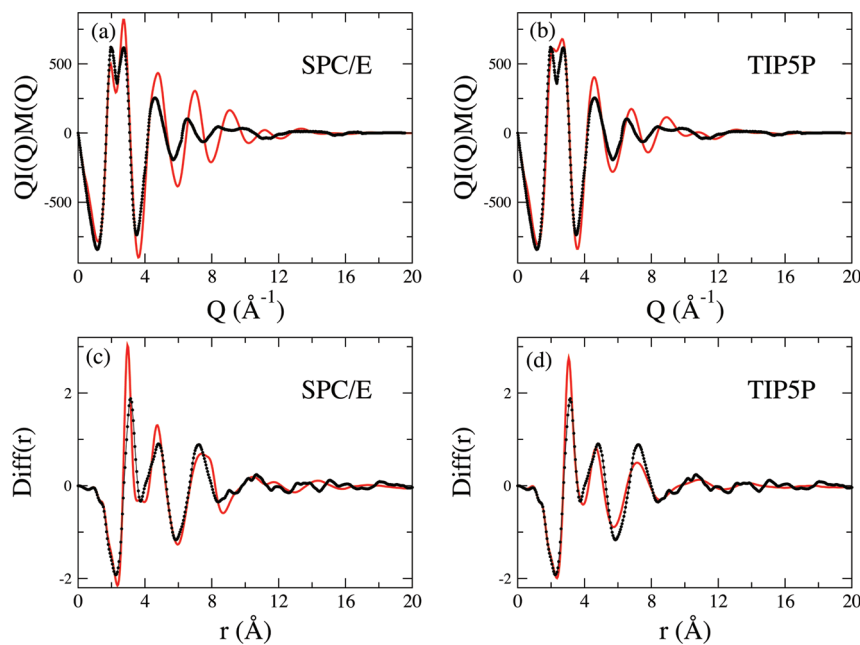


Figure 10. Comparison between the experimental structure factor (dotted black line) and the theoretical one (solid red line) calculated from the SPC/E (a) and TIP5P (b) simulations carried out with the force field parameters reported in the literature. Comparison between the experimental $\text{Diff}(r)$ function (dotted black line) and the theoretical one (solid red line) calculated from the SPC/E (c) and TIP5P (d) simulations carried out with the force field parameters reported in the literature.

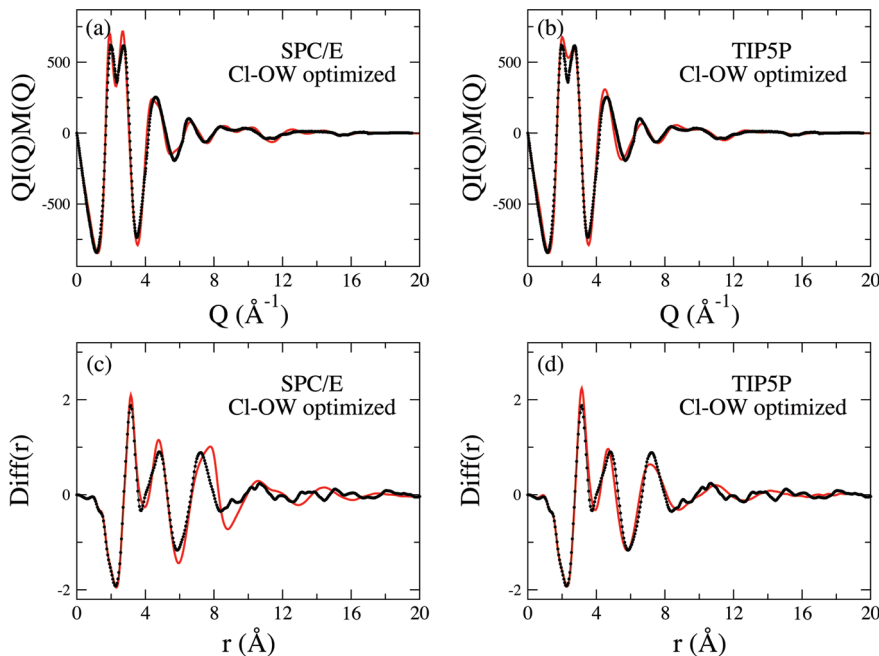


Figure 11. Comparison between the experimental structure factor (dotted black line) and the theoretical one (solid red line) calculated from the SPC/E (a) and TIP5P (b) simulations carried out with the optimized $\sigma_{\text{Cl-OW}}$ values. Comparison between the experimental $\text{Diff}(r)$ function (dotted black line) and the theoretical one (solid red line) calculated from the SPC/E (c) and TIP5P (d) simulations carried out with the optimized $\sigma_{\text{Cl-OW}}$ values.

and long-range interactions among all of the atoms in the system and are only qualitatively reproduced by the theoretical calculations.

For the SPC/E water model, the intensities of the theoretical second and third peaks are overestimated and slightly underestimated, respectively, whereas in the TIP5P case, the theoretical minimum at about 6 Å is too high and shifted toward shorter

distances and the height of the third peak is too low, as compared with the experimental data. However, the larger discrepancies between theory and experiment are found in the first peak region. In particular, the positions of the theoretical first peaks are shifted toward shorter distances (2.95 and 3.05 Å for the SPC/E and TIP5P water model, respectively), and the intensities are much

Table 3. Comparison between the σ Parameters for the Cl–OW Lennard-Jones Potential Obtained from Our Optimization Procedure and That Reported in the Literature^a

	OPLS ⁵⁸	Pálinkás et al. ⁵⁹	Dang et al. ⁶⁰	this work
$\sigma_{\text{Cl}-\text{Cl}}$ (Å)	4.311	4.860	4.455	
$\sigma_{\text{Cl}-\text{OW}}$ SPC/E (Å)	3.738	4.013	3.810	3.618
$\sigma_{\text{Cl}-\text{OW}}$ TIPSP (Å)	3.716	3.990	3.788	3.515

^a The σ values for Cl–Cl Lennard-Jones potential are also reported.

higher than the experimental one, especially in the SPC/E calculation. Due to the strong anion–water interactions, the large scattering factor of chlorine, and the large number of water molecules present in the mixture, the main contributions to the first peak originate from contacts between the chloride ion and the oxygen atoms of water molecules belonging to the Cl^- first coordination sphere, and from oxygen–oxygen interactions between nearest neighbor water molecules.

Both the IL and water force fields were obtained and tested by simulations of the pure components. The disagreement between the theoretical and experimental $\text{Diff}(r)$ first peak points to the need to improve the description of the chloride–water cross interactions. This is not surprising, since the Lennard-Jones parameters for cross interactions in IL/water mixtures do not necessarily follow any simple set of “mixing rules”. For this reason, we have resorted to optimizing the σ parameter of the Cl–OW (OW is the oxygen atom of the water molecule) Lennard-Jones potential to obtain the best possible agreement with the experimental data. We chose this parameter, since the Cl–water first shell distance, which, from the comparison between the theoretical and experimental $\text{Diff}(r)$'s, seems to be underestimated by our MD simulations, critically depends on the $\sigma_{\text{Cl}-\text{OW}}$ value. However, the Cl–water first-shell interactions also depend on the other parameters of the water model, such as partial charges, number, and positions of atomic sites and ϵ parameter of the Cl–OW Lennard-Jones potential. This means that the $\sigma_{\text{Cl}-\text{OW}}$ value that can correctly reproduce the experimental signals might be different for the SPC/E and TIPSP water models. For this reason, σ has been optimized separately for the two MD simulations. The refinement of the σ parameter led to a much better agreement between the theoretical and experimental $I(Q)$'s for both water models (Figure 11a and b).

As far as the $\text{Diff}(r)$ functions are concerned, the position of the experimental first peak at 3.15 Å is perfectly reproduced by the two MD simulations carried out with the optimized $\sigma_{\text{Cl}-\text{OW}}$ values (Figure 11c and d). In the distance range below 5.7 Å, the theoretical SPC/E and TIPSP $\text{Diff}(r)$'s match the experimental data very well, meaning that the local contacts among all of the atoms in the system in a range of \sim 6 Å are correctly reproduced by both water models. A different result has been obtained for the long-range interactions. As can be seen, for distances larger than 5.7 Å, the theoretical $\text{Diff}(r)$ calculated from the TIPSP simulation is in much better agreement with the experimental data, as compared with the SPC/E case, thus showing that the TIPSP water model provides a better description of the long-range structure formed in the EAC/water mixture. It is noteworthy that such a good agreement between theory and experiment has been obtained by modifying a single interaction parameter. This indicates that, with the exception of the Cl–water interactions, the force field is able to provide a very good description of the interactions among all of the atoms in the system. It is important

to stress that we have also explored additional corrections to the force field, concerning the other interaction parameters, but in all cases, we obtained a worse agreement with the experimental data. The $\sigma_{\text{Cl}-\text{OW}}$ values obtained from the optimization procedure are reported in Table 3. Note that the optimized $\sigma_{\text{Cl}-\text{OW}}$ values correspond to an increase of 0.15 and 0.07 Å in the starting ones obtained from the Lorentz–Berthelot combining rules (3.468 and 3.445 Å for the SPC/E and TIPSP models, respectively).

At this point, it is important to compare our optimized $\sigma_{\text{Cl}-\text{OW}}$ parameters with the σ values previously used to describe the Cl–water interactions. Several interaction potentials, which were developed to reproduce thermodynamic or structural properties of aqueous solutions containing the chloride ion,^{58–60} can be found in the literature. Some of them were subsequently used for describing the Cl–water interactions in mixtures of water either with 1,3-dimethylimidazolium chloride¹⁸ or with tetraalkylammonium chloride.⁶¹ The interaction potentials are usually reported in the form of σ parameters for the Cl–Cl Lennard-Jones potential, and Cl–OW cross terms can be calculated as the arithmetic average of $\sigma_{\text{Cl}-\text{Cl}}$ and $\sigma_{\text{OW}-\text{OW}}$ (see Table 3). As can be seen, our $\sigma_{\text{Cl}-\text{OW}}$ parameters are shorter than all of the other ones reported in the table. As previously mentioned, by using our optimized σ 's, the first peak positions of the theoretical $\text{Diff}(r)$ functions are identical to the experimental one. This result could not be obtained if the σ values reported in the literature were used in the calculations. In the latter case, the theoretical $\text{Diff}(r)$ first peak would be shifted toward significantly larger distances, as compared to the experimental data.

For the sake of comparison, note that an increase of only 0.05 Å of our $\sigma_{\text{Cl}-\text{OW}}$ refined for the SPC/E water model resulted in a shift of the SPC/E $\text{Diff}(r)$ first peak to 3.25 Å, which is 0.1 Å longer than the experimental peak position. Altogether, our results show that care must be taken when trying to obtain structural information on IL/water mixtures from MD simulations carried out with commonly used force fields. Many of the force fields that have been proposed have not been subjected to a rigorous validation procedure, especially from a structural point of view. In this respect, the comparison with X-ray diffraction data represents a very tight test on the quality of the potentials used in the calculations, and in our opinion, this comparison should become a common practice to assess the reliability of the structural results obtained from MD simulations.

To gain an overall view of the structural properties of the EAC/water mixture, we have calculated the radial distribution functions $g(r)$'s of a selected subset of atoms. The $g(r)$'s are a common tool to characterize the structure of liquids and their mixtures, through the effective pairwise interaction between two atomic species. All of the calculated $g(r)$'s are depicted in Figure 12a–e, and selected first peak positions are reported in Table 4. We refer to the oxygen and hydrogen atoms of the water molecule as OW and HW.

The Cl–OW and Cl–HW $g(r)$'s calculated from the SPC/E and TIPSP simulations (Figure 12a) show very sharp and distinct first peaks, indicating that strong anion–water interactions are present, in agreement with prevailing concepts.¹⁴ Moreover, in the Cl–HW $g(r)$'s, two peaks are found, the former at shorter distances, and the latter, at longer distances, as compared with the Cl–OW $g(r)$ first maxima. This means that the first-shell water molecules orient only one hydrogen atom toward the chloride. These results are in line with the strong ability of the Cl^- ion to form hydrogen bonds. As concerns the differences between the two water models, the position of the Cl–OW and Cl–HW $g(r)$

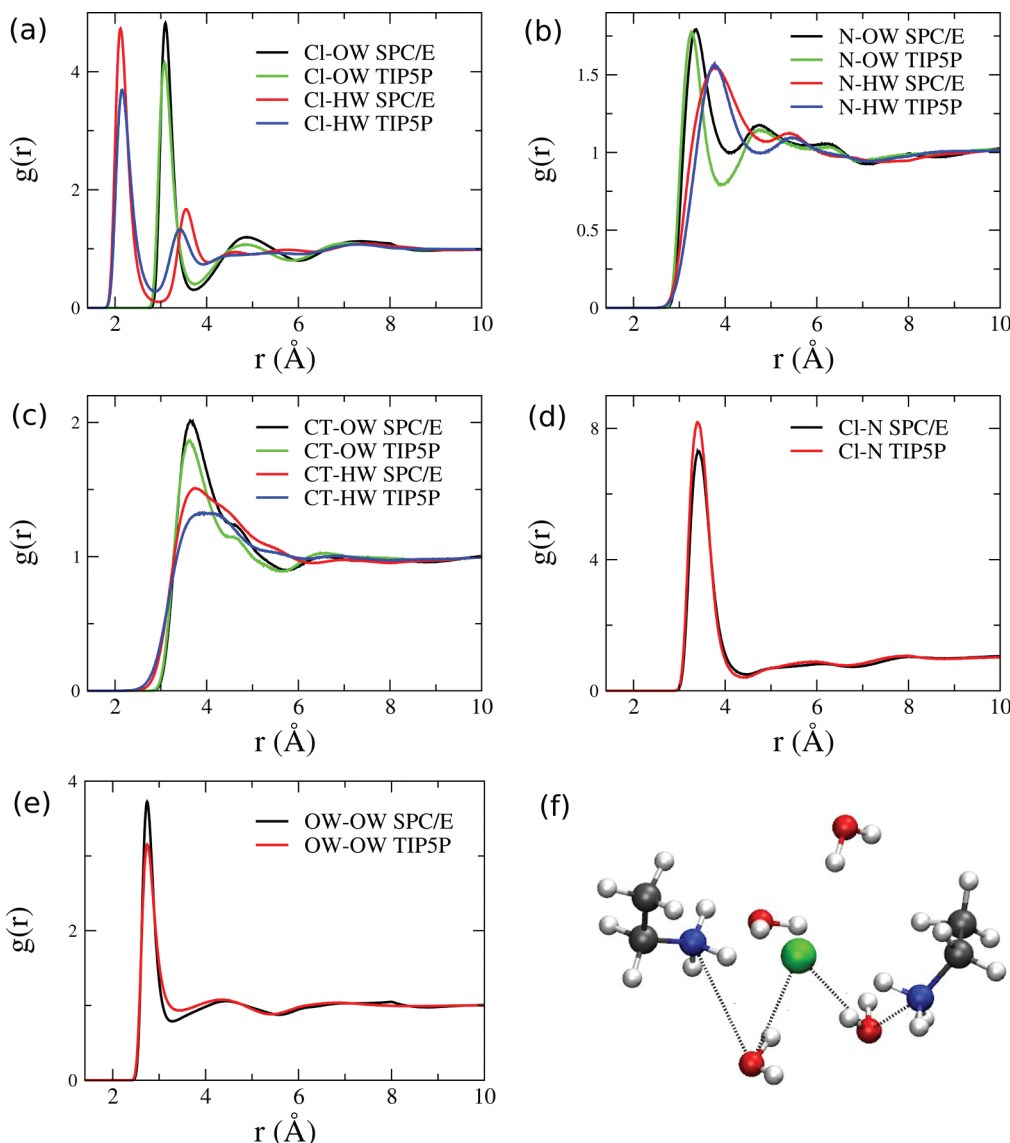


Figure 12. (a–e) Radial distribution functions, $g(r)$'s, of a selected subset of atoms calculated from the SPC/E and TIP5P simulations. OW and HW are the oxygen and hydrogen atoms of the water molecules, and CT is the C atom of the terminal methyl group. (f) Simulation snapshot showing the water molecules and cations belonging to the chloride first coordination sphere. The dashed lines indicate that the water molecules are shared between the anion and the cation.

first peaks are very similar in both trajectories, but their intensities are higher in the SPC/E simulation, indicating a more structured Cl^- first coordination sphere.

The N–OW and N–HW $g(r)$'s (Figure 12b) show that a first hydration shell is formed also around the N atom of the cation, but the peaks are less pronounced as compared with the Cl–water $g(r)$'s, because the cation–water interactions are weaker than the anion–water ones. The first shell water molecules, on average, prefer to orient the oxygen toward the N atom, but in this case, the oxygen and hydrogen $g(r)$ first peaks are not well separated, and a larger orientational freedom is found, as compared with the chloride first hydration shell. As far as the carbon atom of the terminal methyl group is concerned (CT), the positions of the CT–OW and CT–HW $g(r)$ first peaks are quite similar (Figure 12c), thus suggesting an almost tangential arrangement of water molecules in the vicinity of the methyl group. Even if the water molecules strongly interact with

Cl^- and, to a lesser extent, with EA, cations and anions are not completely separated, as shown by the strong Cl–N correlation that is found in both the SPC/E and TIP5P simulations (Figure 12d). Moreover, the high and well-defined short-range peak of the OW–OW $g(r)$ (Figure 12e) suggests that the water molecules in the mixture tend to aggregate and form water clusters.

To better quantify the structural features of the EAC/water system, we have computed a series of coordination numbers. These represent the average number of atoms within a given cutoff distance from the selected reference atom, and they are obtained by the numerical integration of the radial distribution function. For each selected couple of atoms, the cutoff distance has been chosen as the position of the first minimum of the corresponding radial distribution function. The coordination numbers obtained from the two simulations are reported in Table 4, together with the cutoff distances used in the calculations.

Table 4. Structural Parameters of the Radial Distribution Functions, $g(r)$'s, Depicted in Figure 12a–e^a

	R (Å)	N	cutoff distance (Å)
Cl–OW SPC/E	3.10	4.52	3.70
Cl–OW TIPSP	3.08	4.52	3.76
N–OW SPC/E	3.36	4.56	4.00
N–OW TIPSP	3.26	3.83	3.93
CT–OW SPCE	3.64	17.00	5.70
CT–OW TIPSP	3.64	15.40	5.62
Cl–N SPC/E	3.42	1.93	4.45
Cl–N TIPSP	3.40	2.02	4.41
OW–OW SPC/E	2.74	3.08	3.30
OW–OW TIPSP	2.74	3.41	3.40

^a R is the position of the $g(r)$ first peak and N is the coordination number calculated by integration of the $g(r)$. The cutoff distances used in the calculation of N are also reported.

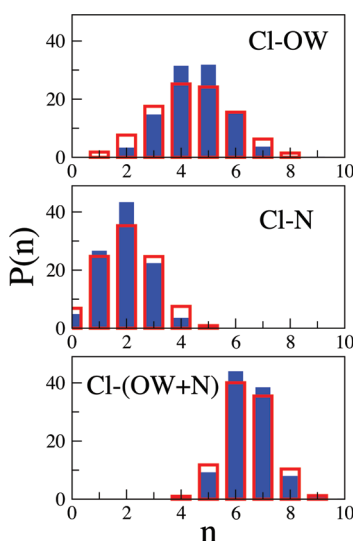


Figure 13. Distributions of the Cl^- instantaneous coordination number (n) calculated for the oxygen atom of the water molecules (Cl–OW), for the N atom of the cations (Cl–N), and for the sum of the oxygen and nitrogen atoms (Cl–(OW + N)). The results obtained from the SPC/E simulation are shown as solid blue bars while the TIPSP ones as empty red bars.

Both in the SPC/E and TIPSP simulations, the first hydration shell of chloride contains ~ 4.5 water molecules. This coordination number is lower than the hydration number of chloride in aqueous solution, which is 6 according to most X-ray and neutron diffraction studies,^{62–65} but is very close to the number of water molecules (4.75) that have been found in the Cl^- first hydration shell in a recent Car–Parrinello simulation of one 1-ethyl-3-methylimidazolium chloride ion pair dissolved in 60 water molecules.⁶⁶ Even if over a larger distance range, a similar number of water molecules are present also in the first coordination shell of the N atom (in the TIPSP case this number is slightly lower), whereas a huge hydration number is obtained for the CT atom, which is due to the very large cutoff distance used in the calculation. The water–water coordination number is almost 3 in the SPC/E simulation and slightly higher in the TIPSP one, but both the SPC/E and TIPSP trajectories predict the presence

of about two cations in the first coordination shell of the anion and vice versa.

A number of snapshots extracted from the trajectories were visualized, and the results obtained from the SPC/E and TIPSP simulations were almost identical. We observed that the cation and anion do not possess a completely closed hydration shell of their own, but rather, “solvent-shared ion pairs” are formed. In particular, one or more water molecules belonging to the first solvation shell of the anion can act as a bridge and thus be shared with the N atom of the cation. A deeper insight into this structural behavior has been gained by defining an instantaneous coordination number, n , of the Cl^- ion as the number of atoms of a certain type (X) at a distance from chloride shorter than the Cl^-X $g(r)$ first minimum (see Table 4) and analyzing its variation along the simulations. In particular, we have calculated the coordination number distributions for the oxygen atom of the water molecules, for the N atom of the cations, and for the sum of the oxygen and nitrogen atoms (see Figure 13). The results of this analysis show that in both trajectories, the Cl^- ion transits among several Cl–O and Cl–N coordination numbers, and the distributions obtained from the TIPSP simulation are slightly broader, as compared with the SPC/E ones. However, for both water models, we have found a dominant percentage of Cl^- first coordination shell containing either six or seven first neighbors; that is, either four or five water molecules and two N atoms of the cation. Moreover, the percentage of Cl^- local environments with no N atoms within the cutoff distance is very low (below 7%) in both simulations.

To provide visual insight, a representative snapshot of the Cl^- first coordination sphere containing four water molecules and two cations is shown in Figure 12f. It can be seen that two water molecules act as a bridge between the anion and the cations, thus belonging to both the first hydration shell of Cl^- and N. The existence of solvent-shared ion pairs in IL/water mixtures has been previously pointed out in the above-mentioned Car–Parrinello simulation study of a 1-ethyl-3-methylimidazolium chloride/water mixture.⁶⁶ Albeit the great excess of water present in the mixture (IL/water molar ratio 1:60), it was found that the cation and anion did not separate from each other but remained in close proximity over the whole simulation time by sharing one or more solvent molecules. Another interesting behavior that emerged from our MD analysis is the preferential formation of clusters of water molecules in the neighborhood of the CT atom, where the water–water distances tend to resemble that of pure water. From these results, we can suppose that also by increasing the concentration of the water molecules present in the mixture, the intruding water would not break up the cation–anion network so that solvent shared ion pairs continue to survive. In such a scenario, the additional water molecules would interact with each other by forming bigger and bigger clusters of water molecules. This can be the subject of a future investigation.

CONCLUSIONS

The presence of a polymorphic transition from a monoclinic LT phase to a tetragonal HT phase has been unequivocally observed at 358 K. Such transformation shows a reconstructive behavior that is different from the order–disorder character hypothesized from Raman spectroscopy.⁴ Thermal expansion of both polymorphs is small and anisotropic as a result of an anisotropic interaction network. The HT phase, space group

$P4/n$ or $P4/nmm$, $a = 5.05 \text{ \AA}$, $c = 9.99 \text{ \AA}$, has an excess volume of $\sim 11\%$ with respect to the LT polymorph. The structure of the nonquenchable HT polymorph has been solved by direct methods on powder diffraction data and refined in the centrosymmetric $P4/nmm$ space group. Significant rotational disorder of the C1 atom has been observed along the N—C2 vector. This finding is consistent with model 1 of rotational reorganization proposed by Radcliffe¹⁰ for the bromide and iodide salts instead of model 2 proposed for EAC. The strongest N···Cl interaction is at a distance of $\sim 3.2 \text{ \AA}$ and is aligned along the c axis, which represents the strongest axis against thermal expansion.

The structural properties of an EAC/water mixture have been investigated here for the first time by combining MD simulations and X-ray diffraction experiments. Two of the most widespread water models—namely, the SPC/E and TIPSP—were used in the calculations, whereas for the ionic liquid, the Lopes-Padua force field was employed. The optimization of a single Lennard-Jones parameter, related to the Cl—water interactions, has allowed us to obtain very good agreement between the theoretical and experimental diffraction patterns. We have found that both water models are able to correctly reproduce the local contacts among all of the atoms in the system in a range of about 6 Å; the TIPSP water model provides a better description of the long-range structure formed in the mixture. A complex structural behavior emerged from the analysis of the trajectories, in which cations and anions are not completely separated, but rather, solvent-shared ion pairs are formed. In particular, the chloride ion is surrounded, on average, by 4.5 water molecules and 2 cations, and one or more water molecules act as a bridge between the anion and the cations. Moreover, the water molecules in the mixture tend to aggregate and form water clusters, especially in the neighborhood of the cation methyl group.

ASSOCIATED CONTENT

S Supporting Information. CIF files of the refinements carried out at the various temperatures are available as Supporting Information. This material is available free of charge via the Internet at <http://pubs.acs.org>.

AUTHOR INFORMATION

Corresponding Author

*E-mail: paolo.ballirano@uniroma1.it.

ACKNOWLEDGMENT

This work was supported by the University of Rome la Sapienza (Progetto Prototipo Ionic Liquids, ateneo 2010). In addition, it was supported by CASPUR with the Standard HPC Grant 2010 entitled: “Structure and dynamics in room temperature ionic liquids”. A.T. acknowledges support from the FIRB “Futuro in Ricerca” research project (RBFR086BOQ_001, “Structure and dynamics of ionic liquids and their binary mixtures”).

REFERENCES

- (1) Wasserscheid, P.; Welton, T., Eds.; *Ionic liquids in synthesis*; Wiley-VCH: Weinheim, 2002.
- (2) Rogers, R. D.; Seddon, K. R., Eds.; *Ionic liquids; Industrial applications for green chemistry*. ACS Symposium Series 818; American Chemical Society: Washington DC, 2002.
- (3) Ratcliffe, C. I.; Sherman, W. I.; Wilkinson, G. R. *J. Raman Spectrosc.* **1982**, *13*, 189.
- (4) Prasad, P. S. R. *J. Phys. Chem.* **1996**, *100*, 888.
- (5) Cambridge Crystallographic Data Centre (CCDC) code ZZZIZM01.
- (6) Jellinek, F. *Acta Crystallogr.* **1958**, *11*, 626.
- (7) Tsau, J.; Gilson, D. F. R. *J. Phys. Chem.* **1968**, *72*, 4082.
- (8) Singh, N. J.; Mitra, S. *Thermochim. Acta* **1992**, *197*, 341.
- (9) Sathaiah, S.; Sarin, V. N.; Bist, H. D. *J. Phys.: Condens. Matter* **1989**, *1*, 7829.
- (10) Ratcliffe, C. I. *Can. J. Chem.* **2004**, *82*, 1517.
- (11) Seddon, K. R.; Stark, A.; Torres, M.-J. *Pure Appl. Chem.* **2000**, *72*, 2275.
- (12) Seddon, K. R.; Stark, A. *Green Chem.* **2002**, *4*, 119.
- (13) Anthony, J. L.; Maginn, E.; Brennecke, J. F. *J. Phys. Chem. B* **2001**, *105*, 10942.
- (14) Cammarata, L.; Kazarian, S. G.; Salter, P. A.; Welton, T. *Phys. Chem. Chem. Phys.* **2001**, *3*, 5192.
- (15) Mele, A.; Tran, C. D.; De Paoli Lacerda, S. H. *Angew. Chem., Int. Ed.* **2003**, *42*, 4364.
- (16) Miki, K.; Westh, P.; Nishikawa, K.; Koga, Y. *J. Phys. Chem. B* **2005**, *109*, 9014.
- (17) Schröder, C.; Rudas, T.; Neumayr, G.; Benkner, S.; Steinhauser, O. *J. Chem. Phys.* **2007**, *127*, 234503.
- (18) Hanke, C. G.; Lynden-Bell, R. M. *J. Phys. Chem. B* **2003**, *107*, 10873.
- (19) Fazio, B.; Triolo, A.; Di Marco, G. *J. Raman Spectrosc.* **2008**, *39*, 233.
- (20) Gontrani, L.; Russina, O.; Lo Celso, F.; Caminiti, R.; Annat, G.; Triolo, A. *J. Phys. Chem. B* **2009**, *113*, 9235.
- (21) Ballirano, P.; Melis, E. *Phys. Chem. Miner.* **2007**, *12*, 289.
- (22) Ballirano, P.; Melis, E. *Phys. Chem. Miner.* **2009**, *36*, 319.
- (23) Ballirano, P.; Melis, E. *Phys. Chem. Miner.* **2009**, *36*, 391.
- (24) Ballirano, P.; Sadun, C. *Struct. Chem.* **2009**, *20*, 815.
- (25) Ballirano, P.; Caminiti, R. *J. Phys. Chem. A* **2009**, *113*, 7774.
- (26) Larson, A. C.; Von Dreele, R. B. *GSAS General Structure Analysis System*; LAUR 86-748; Los Alamos National Laboratory, The Regents of the University of California, 2000.
- (27) Toby, B. H. *J. Appl. Crystallogr.* **2001**, *34*, 210.
- (28) Thompson, P.; Cox, D. E.; Hastings, J. B. *J. Appl. Crystallogr.* **1987**, *20*, 79.
- (29) Finger, L. W.; Cox, D. E.; Jephcoat, A. P. *J. Appl. Crystallogr.* **1994**, *27*, 892.
- (30) Baerlocher, C. H. Restraints and constraints in Rietveld refinement. In *The Rietveld Method*; Young, R. A., Ed.; Oxford Science: Oxford, 1993, Chapter 10.
- (31) Von Dreele, R. B. *J. Appl. Crystallogr.* **1997**, *30*, 517.
- (32) Young, R. A. Introduction to the Rietveld method. In: *The Rietveld Method*; Young, R. A., Ed.; Oxford: Oxford, 1993; pp 1–38.
- (33) Bruker, A. X. S. *Topas V4.2: General profile and structure analysis software for powder diffraction data*; Bruker AXS: Karlsruhe, Germany, 2009.
- (34) Werner, P. E.; Eriksson, L.; Westdahl, M. *J. Appl. Crystallogr.* **1985**, *18*, 367.
- (35) de Wolff, P. M. *J. Appl. Crystallogr.* **1968**, *1*, 108.
- (36) Smith, G. S.; Snyder, R. L. *J. Appl. Crystallogr.* **1979**, *12*, 60.
- (37) Caminiti, R.; Sadun, C.; Rossi, V.; Cilloco, F.; Felici, R. Patent No. 01261484; June 23, 1993.
- (38) Rossi Albertini, V.; Bencivenni, L.; Caminiti, R.; Cilloco, F.; Sadun, C. *J. Macromol. Sci. Phys. B* **1996**, *35*, 199.
- (39) Atzei, D.; Ferri, T.; Sadun, C.; Sangiorgio, P.; Caminiti, R. *J. Am. Chem. Soc.* **2001**, *123*, 2552.
- (40) Carbone, M.; Caminiti, R.; Sadun, C. *J. Mater. Chem.* **1996**, *6*, 1709.
- (41) Abis, L.; Dell'Amico, D. B.; Busetto, C.; Calderazzo, F.; Caminiti, R.; Ciolfi, C.; Garbassi, F.; Mascarelli, G. *J. Mater. Chem.* **1998**, *8*, 751.
- (42) Smith, W.; Forester, T. *J. Mol. Graphics* **1996**, *14*, 136.

- (43) Frisch, M. J.; Trucks, G. W.; Schlegel, H. B.; Scuseria, G. E.; Robb, M. A.; Cheeseman, J. R.; Montgomery, J. A., Jr.; Vreven, T.; Kudin, K. N.; Burant, J. C.; Millam, J. M.; Iyengar, S. S.; Tomasi, J.; Barone, V.; Mennucci, B.; Cossi, M.; Scalmani, G.; Rega, N.; Petersson, G. A.; Nakatsuji, H.; Hada, M.; Ehara, M.; Toyota, K.; Fukuda, R.; Hasegawa, J.; Ishida, M.; Nakajima, T.; Honda, Y.; Kitao, O.; Nakai, H.; Klene, M.; Li, X.; Knox, J. E.; Hratchian, H. P.; Cross, J. B.; Bakken, V.; Adamo, C.; Jaramillo, J.; Gomperts, R.; Stratmann, R. E.; Yazyev, O.; Austin, A. J.; Cammi, R.; Pomelli, C.; Ochterski, J. W.; Ayala, P. Y.; Morokuma, K.; Voth, G. A.; Salvador, P.; Dannenberg, J. J.; Zakrzewski, V. G.; Dapprich, S.; Daniels, A. D.; Strain, M. C.; Farkas, O.; Malick, D. K.; Rabuck, A. D.; Raghavachari, K.; Foresman, J. B.; Ortiz, J. V.; Cui, Q.; Baboul, A. G.; Clifford, S.; Cioslowski, J.; Stefanov, B. B.; Liu, G.; Liashenko, A.; Piskorz, P.; Komaromi, I.; Martin, R. L.; Fox, D. J.; Keith, T.; Al-Laham, M. A.; Peng, C. Y.; Nanayakkara, A.; Challacombe, M.; Gill, P. M. W.; Johnson, B.; Chen, W.; Wong, M. W.; Gonzalez, C.; Pople, J. A. *Gaussian 03, Revision C.02*, Gaussian, Inc., Wallingford CT, 2004.
- (44) Breneman, C. M.; Wiberg, K. B. *J. Comput. Chem.* **1990**, *11*, 361.
- (45) Canongia Lopes, J. N.; Pádua, A. A. H. *J. Phys. Chem. B* **2004**, *108*, 16893.
- (46) Canongia Lopes, J. N.; Deschamps, J.; Pádua, A. A. H. *J. Phys. Chem. B* **2004**, *108*, 2038.
- (47) Berendsen, H. J. C.; Grigera, J. R.; Straatsma, T. P. *J. Phys. Chem.* **1987**, *91*, 6269.
- (48) Mahoney, M. W.; Jorgensen, W. L. *J. Chem. Phys.* **2000**, *112*, 8910.
- (49) Evans, D. J.; Holian, B. L. *J. Chem. Phys.* **1985**, *83*, 4069.
- (50) Nosé, S. *J. Chem. Phys.* **1984**, *81*, 511.
- (51) Pings, C. J.; Waser, J. *J. Chem. Phys.* **1968**, *48*, 3016.
- (52) Berendsen, H. J. C.; van der Spoel, D.; van Drunen, R. *Comput. Phys. Commun.* **1995**, *91*, 43.
- (53) *Mercury 2.3*; Cambridge Crystallographic Data Centre, 12 Union Road, Cambridge, England 2002.
- (54) Fei, Y. Thermal expansion. In *Mineral physics and crystallography: A handbook of physical constants*; Ahrens, T. J., Ed.; American Geophysical Union: Washington, DC, 1995; Vol 2; pp 29–44.
- (55) Choi, C. S.; Prask, H. J. *Acta Crystallogr.* **1983**, *B39*, 414.
- (56) Altomare, A.; Burla, M. C.; Camalli, M.; Carrozzini, B.; Cascarano, G.; Giacovazzo, C.; Guagliardi, A.; Moliterni, A. G. G.; Polidori, G.; Rizzi, R. *J. Appl. Crystallogr.* **1999**, *32*, 339.
- (57) Altomare, A.; Burla, M. C.; Camalli, M.; Cascarano, G.; Giacovazzo, C.; Guagliardi, A.; Moliterni, A. G. G.; Polidori, G.; Spagna, R. *J. Appl. Crystallogr.* **1999**, *32*, 115.
- (58) Chandrasekhar, J.; Spellmeyer, D. C.; Jorgensen, W. L. *J. Am. Chem. Soc.* **1984**, *106*, 903.
- (59) Pálinkás, G.; Riede, O.; Heinzinger, K. *Z. Naturforsch. A* **1977**, *32*, 1197.
- (60) Dang, L. X.; Smith, D. E. *J. Chem. Phys.* **1993**, *99*, 6950.
- (61) Krienke, H.; Vlachy, V.; Ahn-Ercan, G.; Bakó, I. *J. Phys. Chem. B* **2009**, *113*, 4360.
- (62) Caminiti, R.; Licheri, G.; Piccaluga, G.; Pinna, G.; Radnai, T. *J. Chem. Phys.* **1979**, *71*, 2473.
- (63) Caminiti, R.; Licheri, G.; Paschina, G.; Piccaluga, G.; Pinna, G. *Z. Naturforsch.* **1980**, *35a*, 1361.
- (64) Caminiti, R.; Musinu, A.; Paschina, G.; Pinna, G. *J. Appl. Crystallogr.* **1982**, *15*, 482.
- (65) Ohtaki, H.; Radnai, T. *Chem. Rev.* **1993**, *93*, 1157.
- (66) Spickermann, C.; Thar, J.; Lehmann, S. B. C.; Zahn, S.; Hunger, J.; Buchner, R.; Hunt, P. A.; Welton, T.; Kirchner, B. *J. Chem. Phys.* **2008**, *129*, 104505.